November 13, 2014

Fracture and Structural Integrity
Journals Department

To whom it may concern:

Please find enclosed the manuscripts entitled: **THE INFLUENCE OF FIBRE ORIENTATION ON THE POST-CRACKING TENSILE BEHAVIOUR OF STEEL FIBRE REINFORCED SELF-COMPACTING CONCRETE by** Amin Abrishambaf, Vitor Cunha, Joaquim Barros**.** The authors confirm the manuscript is an original version and has not been published elsewhere**.**

We would like to have this manuscript published by the **Fracture and Structural Integrity Journal.**

Should you need to contact me, please use the following information:
Tel: **+351 253 510 210**
Fax: **+351 253 510 217**
Email: **vcunha@civil.uminho.pt**

Address:

Universidade do Minho

Departamento de Engenharia Civil, ISISE

Campus de Azurém

4800-058 Guimarães

PORTUGAL

Sincerely,
Vitor Cunha
(the corresponding author)

THE INFLUENCE OF FIBRE ORIENTATION ON THE POST-CRACKING TENSILE BEHAVIOUR OF STEEL FIBRE REINFORCED SELF-COMPACTING CONCRETE

A. Abrishambaf [1], V.M.C.F. Cunha[1*], J.A.O. Barros [1]

[1] ISISE, Dep. Civil Eng., School Eng., University of Minho, Campus de Azurém 4800-058 Guimarães, Portugal.

ABSTRACT

Adding fibres to concrete provides several advantages, especially in terms of controlling the crack opening width and propagation after the cracking onset. However, distribution and orientation of the fibres toward the active crack plane are significantly important in order to maximize its benefits. Therefore, in this study, the effect of the fibre distribution and orientation on the post-cracking tensile behaviour of the steel fibre reinforced self-compacting concrete (SFRSCC) specimens is investigated. For this purpose, several cores were extracted from distinct locations of a panel and were subjected to indirect (splitting) and direct tensile tests. The local stress-crack opening relationship (σ-w) was obtained by modelling the splitting tensile test under the finite element framework and by performing an Inverse Analysis (IA) procedure. Afterwards the σ-w law obtained from IA is then compared with the one ascertained directly from the uniaxial tensile tests. Finally, the fibre distribution/orientation parameters were determined adopting an image analysis technique.

KEYWORDS: Fibre dispersion and orientation, Self-compacting concrete, Tensile behaviour, Splitting tensile test, Inverse analysis.

[*] Correspondent author. Tel.: +351 253510210   E-mail address: vcunha@civil.uminho.pt

1. INTRODUCTION

Adding fibres to concrete provides several advantages, especially in terms of controlling the crack opening width and propagation, increasing the energy absorption capacity, as well as increasing the post-cracking tensile strength [1, 2]. In composites reinforced with low fibre contents, the contribution of the fibres mainly arises after the crack initiation. Crack opening in steel fibre reinforced concrete (SFRC) is restrained by the bond stresses that develop at the fibre / matrix interface during the fibre pull-out. Moreover, one of the most important properties of SFRC is its ability to transfer stresses across a cracked section rather uniformly, which depends on the fibre reinforcement effectiveness, i.e. fibre properties (their strength, bond and stiffness), and fibre distribution/orientation towards the active crack plane [3].

In order to optimize the fibre contribution to the post-cracking behaviour, it is important to enhance the distribution and orientation of the fibres at the crack plane. Since, fibres are more effective fairly aligned along the principal tensile stresses directions [4, 5]. The dispersion and orientation of fibres in the SFRC bulk hardened-state results from a series of stages, namely [6]: fresh-state properties after mixing; casting conditions into the formwork; flowability properties; and wall-effect introduced by the formwork. Among the aforementioned parameters, flowability of steel fibre reinforced self-compacting concrete (SFRSCC) is the most important one [7-9]. Having in mind that distribution/orientation of the fibres influences significantly the mechanical properties of the SFRSCC, it is important to control and consider both parameters, especially in terms of the design applications.

In this research, the effect of fibre distribution and orientation on the tensile behaviour of a SFRSCC panel is investigated. For this purpose, a total number of 46 cores were extracted from various locations of two panels. These cores were subjected to indirect (splitting) and direct (uniaxial) tensile tests. In order to assess the influence of fibre distribution/orientation on the tensile post-cracking parameters, specimens were notched either parallel or perpendicular to the expected concrete flow direction. Furthermore, fibre distribution parameters were evaluated through an image analysis procedure. Finally, the local stress-crack opening relationship ($\sigma – w$) was obtained by modelling the splitting tensile test under the finite element framework and by performing an Inverse Analysis (IA) procedure. Afterwards the σ-w law obtained from IA is then compared with the one ascertained directly from the uniaxial tensile tests.

2. EXPERIMENTAL PROGRAM

2.1 Concrete mixture

A steel fibre reinforced self-compacting concrete was design with 60 kg/m³ of hooked-end steel fibres (length, l_f, of 33 mm; diameter, d_f, of 0.55 mm; aspect ratio, l_f/d_f, of 60 and a yield stress of 1100 MPa).The mixture constituents are: cement (C), water (w), limestone filler (F), fine sand (FS), coarse sand (CS), coarse aggregate (CA) and superplasticizer (SP). Table 1 includes the adopted concrete mix composition. In order to evaluate the flowability of the concrete, the slump test was performed according to the EFNARC recommendations [10]. The total spread achieved on the slump test was about 670 mm. The Young's modulus and compressive strength were assessed on cylinders with a diameter of 150 mm and height of 300 mm. The average compressive strength (f_{cm}) and the average value of the Young's modulus (E_{cm}) were 47.77 MPa (7.45%) and 34.15 GPa (0.21%), respectively, in which the values in parentheses represent the coefficient of variation.

2.2. Specimens

According to Barnett *et al.* [11] casting panels from its centre point can improve the mechanical behaviour, when comparing to other casting methods. Thus this method was selected for the production of two panels. The dimensions of the panels were 1600×1000×60 mm³. In order to evaluate the influence of fibre dispersion and orientation on the tensile properties of the SFRSCC, twenty three cores were extracted from each panel, and submitted to either indirect (splitting) or direct (uniaxial) tensile tests. The specimens were extracted according to the scheme represented in Fig. 1. In this figure the pale dash lines with arrows represent the supposed concrete flow directions. The hatched cores were used in the splitting tensile tests and the remaining was used in the uniaxial tensile tests. For the execution of the splitting tensile tests, two notches were executed on the cores' opposite sides with the depth of 5 mm. In order to evaluate the influence of crack orientation towards the concrete flow, specimens were notched either parallel or perpendicular toward the expected flow direction. By assuming θ as the angle between the notched plane and the direction of the concrete flow, the notch plane was designated parallel for $\theta = 0^{\circ}$ or perpendicular for $\theta = 90^{\circ}$. Since the core scheme was maintained for both panels, for each core location within the panel there were two cores with distinct notch directions, i.e. $\theta = 0$ or 90º. This will enable to evaluate the influence of fibre orientation on the stress-crack width (σ-w) relationship. For instance, θ of A1 specimen is 90° and 0° in panels A and B, respectively (see Fig. 1).

4

Twenty two cores were sawn to produce prismatic specimens to be used in the uniaxial tensile test with the dimensions of $110 \times 102 \times 60$ mm^3. Following the same notching procedure for the splitting test specimens, the prismatic specimens were notched according to parallel ($\theta = 0°$) and perpendicular ($\theta = 90°$) directions regarding the expected concrete flow. The notch was executed on the four lateral faces of the specimen, at their mid-height, with a thickness of 2 mm and a depth of 5 mm.

2.3 Test setup

2.3.1 Splitting tensile test

In a first stage, the $\sigma - w$ relationship was assessed by carrying out splitting tensile tests. The recommendations of ASTM C-496 standard [12] were followed for this purpose. The tests were executed by closed-loop displacement control. To ensure a proper constant displacement rate, once the crack is initiated, a rather low value of the displacement rate, i.e. 0.001 mm/s, was applied. The crack opening width was averaged from the readouts of five linear variable differential transducers, LVDTs, which were mounted on the surface of the specimen, three on the top and two on the bottom surfaces, see Fig. 2.

2.3.2 Uniaxial tensile test

The stress – crack opening width ($\sigma - w$) relationship was also directly ascertained through uniaxial tensile tests, which were executed according to the RILEM TDF-162 [13]. This test was carried under closed-loop displacement control, adopting the following displacement rates during the test: 0.005 mm/min up to a displacement of 0.05 mm, 0.02 mm/min up to a displacement of 0.1 mm, 0.08 mm/min up to a displacement of 0.5 mm, and 0.1 mm/min until the completion of the test. The test was controlled by the averaging signal received from the four LVDTs installed on the lateral surface of each prismatic specimen, see Fig. 3.

2.4 Results and discussion

2.4.1 Splitting tensile test

Fig. 4 depicts both the envelope and average force – crack mouth opening response ($F – w$) obtained from the splitting tensile tests, when the notch direction was parallel ($\theta = 0^{\circ}$) and perpendicular ($\theta = 90^{\circ}$) to the concrete flow direction. During the first phase of the test, the F - w relationships were almost linear up to the load at the crack onset, since the LVDTs recorded the elastic deformation of the SFRSCC specimen. Therefore this deformation should have been removed from the F - w curves, however since this deformation was marginal it could be neglected. After the crack onset, two distinct behaviours were observed for the $\theta = 0^{\circ}$ and 90° series. Regarding the $\theta = 0^{\circ}$ series (Fig. 4(a)), the composite exhibited a non-linear hardening behaviour until the peak load was attained, followed by a softening phase. On the other hand, for $\theta = 90^{\circ}$ series it was observed just a softening phase immediately after the crack onset. Briefly, these differences between the $\theta = 0^{\circ}$ and 90° series could be ascribed to rather distinct number of fibres intersecting the crack plane at the specimens' notch, due to a preferential fibre alignment perpendicular to the concrete flow direction. The higher number of fibres at the crack plane of the $\theta = 0^{\circ}$ series specimens will promote a higher stress transfer grade between the crack surfaces and, consequently, higher post-cracking residual forces. The aspects related to the fibre distribution / orientation will be detailed further ahead.

In general, the $F – w$ relationship showed a high scatter. However, in the case of SFRSCC the scattering in the results was expected since the mechanical behaviour of this material was significantly dependent on the fibre dispersion/orientation, even for specimens with same geometry and from the same batch. Moreover, in this particular case the relatively high scatter could also be enhanced because the specimens were extracted from different locations of the panels, i.e. with distinct distances from the casting point. Note that during the casting of the panels, the fibre distribution /orientation was influenced by the viscosity and velocity of the fresh concrete along the flowing process.

Figs 5(a) and 5(b) show three average $F – w$ relationships obtained with the splitting tensile test for specimens from the $\theta = 0^{\circ}$ and 90° series, respectively. The "Average" curve was obtained by averaging the readouts of the five LVDTs mounted on the specimen, whereas the "Top" and "Bottom" curves were obtained by averaging only the readouts of the LVDTs mounted, respectively, at the upper and lower specimen's surface. From Fig. 5 it was visible

that the readouts of the LVDTs mounted on the upper surface of specimens showed a relatively higher crack opening width compared to the one recorded by the LVDTs at the lower specimen surface. This denotes that the crack opened asymmetrically, which could be ascribed to the variation of effective fibres along the depth of the panel due to segregation. This aspect will be detailed further ahead, when the fibre distribution parameters are endorsed.

2.4.2 Uniaxial tensile test

Figs 6(a) and 6(b) illustrate the average and envelope force-crack mouth opening relationship obtained from the uniaxial tensile test for the $\theta = 0°$ and $90°$ series, respectively. The value of the crack opening was determined by averaging the readouts of the four LVDTs. For both series ($\theta = 0°$ and $90°$), the F - w curve was almost linear up to the crack initiation. After the crack onset, two distinct behaviours were observed for the $\theta = 0°$ and $90°$ series similarly to what was observed in splitting tensile tests, which could also be ascribed to the distinct number of fibres at the crack plane.

Regarding the $\theta = 0°$ series, fibres start to be slowly pulled-out being observed a semi-hardening response after the crack onset. Afterwards a plateau response was observed until a crack width of about 0.6 mm, and finally it was followed by a smooth reduction in the residual forces. Actually, during the uniaxial tensile testing of the $\theta = 0°$ specimens, once the peak load was achieved the sound of the fibre rupturing was clearly heard, which caused a rapid reduction in the value of the residual forces. This was also confirmed by inspecting the fracture surface visually after the specimen testing. Based on pull-out tests of hooked end fibres [14], fibre rupture may occur between the slip intervals of 0.6-1.0 mm, for the fibre inclination angle with the loading direction of $30°$. As it will be discussed further ahead, for this series the most probable fibre orientation angle towards the cracking plane was around about 35°, this value was derived from the orientation probability distribution ascertained from an image analysis procedure.

On the other hand, the $\theta = 90°$ series, after the crack initiation, shown a sudden force decrease up to a crack width of nearby 0.07 mm followed by a plateau. Cunha *et al.* [5] assessed the micro-mechanical behaviour of hooked end fibres by performing fibre pull-out test. It was verified that after a fibre sliding of nearby 0.1 mm, the fibre

reinforcement mechanism was mainly governed by the hook plasticization during the fibre pull-out process. Additionally, in some specimens of the $\theta = 90°$ series, in particular those located closer to the casting point, shown a pseudo-hardening behaviour as it can be observed by the upper bound of the experimental envelope (Fig. 6(b)). Afterwards, beyond a crack width of about 0.9 mm, a reduction of the residual force was observed, which corresponded to the fibre rupture.

2.4.3 Evaluation of fibre distribution parameters

In order to assess the distribution and orientation of fibres, an image analysis technique was implemented due to its simplicity and relatively low cost [15, 16]. This technique comprised of four main stages: in the first stage, the fracture surface of the specimen was grinded. Then the surface was polished by acetone in order to increase the reflective properties of steel fibres. Secondly, by using a high resolution digital photograph camera, a coloured image of the grinded surface was obtained. Finally, the achieved image was analysed using ImageJ [17] software to recognize steel fibres. The analysis procedure of an image was depicted in Fig.7. After analysing the results, the following parameters were derived out:

i) number of fibres per unit area, N^f : is the ratio between the total number of fibres counted in the image, N_T^f , and the total area of the image, A:

$$N^f = N_T^f \big/ A \tag{1}$$

ii) fibre orientation factor, η_θ : determined as the average orientation towards a certain plane surface by Eq. 2:

$$\eta_\theta = \frac{1}{N_T^f} . \sum_{i=1}^{N_T^f} \cos\theta_i \tag{2}$$

where, N_T^f is the total number of fibres that can be determined by counting all the visible ellipses and circles at the cross section, θ is the out-plane angle that is defined as the angle between the fibre's longitudinal axis and a vector orthogonal to the plane.

iii) fibre segregation parameter, ξ_{seg} : to calculate the location of the steel fibres gravity centre, an average value of the coordinates in the Y axis of entire fibres should be determined in the analysed cross-section.

$$\xi_{seg} = \frac{1}{h.N_T^f} \cdot \sum_{i=1}^{N_T^f} \overline{y} \tag{3}$$

In this equation, $\overline{y}$ is the coordinate in the Y axis of the fibre's gravity centre, and h is the height (or depth) of the analysed cross-section,

iv) number of effective fibres per unit area, N_{eff}^f: the summation of fibres with deformed hooked in a unit area. Since this parameter cannot obtain from the image analysis results, therefore it was executed by visual inspection of the fracture surface.

Table 2 includes the results of the image analysis performed on a plane surface of the uniaxial tensile specimens, see Fig. 8. The fibre distribution parameters were assessed on two orthogonal planes for each core location regarding to panel centre point (Fig. 1). The $\theta = 0^{°}$ series presented a considerably higher average N^f and N_{eff}^f, about 80% and 254%, respectively, when compared to the $\theta = 90^{°}$ series. The differences between these series corroborate that the fibres were preferentially reoriented due to the concrete flow. This could be clearly noticed if the orientation parameter, η_θ, for each series was compared (see Table 2). On the other hand, when the notch plane was parallel to concrete flow direction, a higher orientation factor observed comparing to specimens with $\theta = 90^{°}$. Therefore, in $\theta = 0^{°}$ series, a higher number of the effective fibres in the fracture surface was appeared which increased the concrete fracture parameters. Regarding the fibre segregation factor, the obtained average values of ξ_{seg} were insignificantly higher than 0.5 meaning that a slight fibre segregation occurred through the panel's depth. This could also justify the asymmetric crack opening width observed in the splitting tensile specimens.

Fig. 9 illustrates the orientation profiles obtained for each average orientation factor in comparison to both the two-dimensional (2D) distribution, $\eta_\theta = 2/\pi$, [18] and the three-dimensional (3D) isotropic uniform random fibre distribution, $\eta_\theta = 0.5$, [19]. It was shown that the fibre orientation profile followed a Gaussian distribution [20, 21]. The orientation profile for $\theta = 0^{°}$ series was represented by a distribution shifted to the left side, while for $\theta = 90^{°}$ series the distribution profile tends to the right side. Therefore, within the specimens of $\theta = 0^{°}$ series, fibres have a tendency to be aligned more perpendicular to the studied plane. The obtained distribution profile for the $\theta = 0^{°}$ series

was completely distinct from either the 2*D* or 3*D* theoretical isotropic uniform random distributions. Meanwhile, the distribution obtained for the $\theta = 90^{\circ}$ series was very similar to the 2*D* theoretical distribution. In conclusion, for SFRSCC laminar structures, assuming a 2*D* or 3*D* uniform fibre random distribution may be far from the reality, since the influence of fibre orientation due to the concrete flow also needs to be taken in to the account. Fig. 10 shows the exponential relationship between the number of fibres, N^f, and effective fibres, N^f_{eff}.

3. NUMERICAL SIMULATION

The most suited test to derive the mode I fracture parameters is the uniaxial tensile test. However, the latter test involves some difficulties such as: the necessity of specialized and expensive equipment; sophisticated test set-up to avoid detrimental interferences, like load eccentricity, since it decreases the stress at the onset of crack initiation [22]. On the other hand the splitting tensile test could be considered as an alternative option for this purpose, because it is cheaper, less sophisticated testing equipment is needed, and can be executed on both cubes and extracted cores.

In this section a methodology to predict the stress – crack width (σ – w) relationship of SFRSCC using an inverse analysis, IA, procedure based on the results of the splitting tensile test will be presented and discussed. For this purpose, numerical simulations of the splitting tensile tests were carried out with a nonlinear 3*D* finite element model. In order to confirm the accuracy of the proposed methodology, the σ – w response obtained through the IA of the splitting test results was compared to the σ – w response obtained from the uniaxial tensile test.

3.1 Modelling and simulation

The average experimental force – crack width responses of the splitting tensile tests (Fig. 4) were simulated using ABAQUS® finite element software [23]. Eight-node hexahedral shape solid elements with 8-integration points were used. The concrete damage plasticity model was implemented in order to simulate mechanical properties of concrete [24, 25]. Because of the symmetry in the specimen geometry, supports and test loading applied in the splitting tensile test, only a quarter of the core was simulated, see Fig. 11(a). Since the specimen had distinct thicknesses it consists of two main parts namely: Notch and Un-notch (flush). After meshing each part individually, the assembled

mesh is shown in Fig. 11(b) with a total number of 5674 elements. Similar to the performed in the experimental procedure, in the numerical simulation a prescribed displacement was applied on top of the notch.

3.2 Concrete constitutive model

The concrete damage plasticity, CDP, model was used to simulate the mechanical performance of concrete because it is proficient to model the cracking of concrete in tension and crushing in compression. On the other hand, this model uses the concept of isotropic damage elasticity in combination with isotropic compression and tension plasticity to simulate the inelastic behaviour of concrete under compressive and tensile stresses. The CDP model uses a yield surface that is defined as the loading function proposed by Lubliner *et al.* [26]. The evaluation of the yield surface is controlled by two hardening variables, namely, the plastic strain in tension ($\tilde{\varepsilon}_t^{pl}$) and the plastic strain in compression ($\tilde{\varepsilon}_c^{pl}$). In the case of the effective stress, the yield function is determined as follow:

$$F = \frac{1}{1-\alpha}\left(\bar{q} - 3\alpha\bar{p} + \beta\left(\tilde{\varepsilon}^{pl}\right)\left\langle\hat{\bar{\sigma}}_{\max}\right\rangle - \gamma\left\langle-\hat{\bar{\sigma}}_{\max}\right\rangle\right) - \bar{\sigma}_c\left(\tilde{\varepsilon}_c^{pl}\right) \tag{4}$$

where:

$$\alpha = \frac{\left(\sigma_{b0}/\sigma_{c0}\right)-1}{2\left(\sigma_{b0}/\sigma_{c0}\right)-1} \quad , \qquad 0 \leq \alpha \leq 0.5 \tag{5}$$

$$\beta = \frac{\bar{\sigma}_c\left(\tilde{\varepsilon}_c^{pl}\right)}{\bar{\sigma}_t\left(\tilde{\varepsilon}_t^{pl}\right)}\left(1-\alpha\right)-\left(1+\alpha\right) \tag{6}$$

$$\gamma = \frac{3\left(1-k_c\right)}{2k_c-1} \tag{7}$$

In these equations, $\bar{p}$ and $\bar{q}$ are two stress invariants of the effective stress tensor, namely, the hydrostatic stress and the Von Mises equivalent effective stress, respectively, $\hat{\bar{\sigma}}_{\max}$ stands for the maximum principal effective stress and is the algebraic maximum eigen value of the effective stress $\bar{\sigma}$ [27], $\left\langle x \right\rangle$ represents Macauley bracket $= 1/2\left(|x|+x\right)$, σ_{b0}/σ_{c0} is the ratio between the initial biaxial compressive strength and the initial uniaxial compressive strength, $\bar{\sigma}_t(\tilde{\varepsilon}_t^{pl})$ and $\bar{\sigma}_c(\tilde{\varepsilon}_c^{pl})$ are the effective tensile and compressive cohesive stresses, respectively. Parameter k_c is physically assumed as a ratio of the distances between, respectively, the compressive meridian and

11

the tensile meridian with hydrostatic axis in the deviatoric cross section. If this ratio tends to 1, the deviatoric cross section of the failure surface becomes a circle similar to the Drucker – Prager yielding surface. However, definition of this parameter is only possible if the full triaxial compressive tests are executed on concrete specimens [28]. Tables 3 include the adopted initial parameters for the CDP model used to simulate the response of the splitting tensile tests.

3.2.1 Stress – strain relationship for modeling the SFRSCC uniaxial compressive behaviour

In CDP model, once the concrete compressive strength ($\sigma_{cu} = f_{cm}$) attained, the concrete shifts to the non-linear phase. Then, the compressive inelastic strain, $\tilde{\varepsilon}_c^{in}$, is defined by subtracting the elastic strain component, ε_{0c}^{el}, from the total strain, ε_c, in the uniaxial compressive test.

$$\tilde{\varepsilon}_c^{in} = \varepsilon_c - \varepsilon_{0c}^{el} \tag{8}$$

$$\varepsilon_{0c}^{el} = \sigma_c / E_0 \tag{9}$$

In the CDP model, from the stress – inelastic strain relationship ($\sigma_c - \tilde{\varepsilon}_c^{in}$) that is provided by the user, the stress versus strain response ($\sigma_c - \varepsilon_c$) can be converted to the stress – plastic strain curve ($\sigma_c - \tilde{\varepsilon}_c^{pl}$) automatically by the software. Table 4 includes the values of the model parameters used in the numerical simulation of the splitting tensile tests.

3.2.2 Stress – strain relationship for modeling the SFRSCC uniaxial tensile behaviour

The stress – strain response under uniaxial tension had a linear elastic behaviour until the material tensile strength (σ_{t0}) was attained. Afterward, the tensile response shifted to the post-cracking phase where a non-linear response was assumed. The SFRC post-cracking strain, $\tilde{\varepsilon}_t^{ck}$, can be determined by subtracting the elastic strain, ε_{0t}^{el}, corresponding to the undamaged part from the total strain, ε_t:

$$\tilde{\varepsilon}_t^{ck} = \varepsilon_t - \varepsilon_{0t}^{el} \tag{10}$$

$$\varepsilon_{0t}^{el} = \sigma_t / E_0 \tag{11}$$

12

From the stress – cracking strain response ($\sigma_t - \tilde{\varepsilon}_t^{ck}$) defined by the user, the stress – strain curve ($\sigma_t - \varepsilon_t$) was converted to a stress – plastic strain relationship ($\sigma_t - \tilde{\varepsilon}_t^{pl}$).

3.3 Inverse analysis procedure

The σ_i and w_i values that define the tensile stress – crack width law were computed by fitting the numerical load – crack width curve to the correspondent experimental average curve. From the nonlinear finite element analysis, the numerical load – crack width response, $F_{NUM} - w$, was determined, and compared to the experimental one, $F_{EXP} - w$. At last the normalized error, *err*, was computed as follows:

$$err = \sum_{i=0}^{w_u} \left| F_{iEXP} - F_{iNUM} \right| \bigg/ \sum_{i=0}^{w_u} F_{iEXP} \tag{12}$$

where F_{iEXP} and F_{iNUM} were the experimental and the numerical load value at i^{th} crack width value, respectively. The final $\sigma - w$ relationship was defined by the parameters set that lead to the lowest normalised error between the experimental and numerical compressive force versus crack width curves.

3.4 Numerical results

Fig. 12 illustrates the numerical response obtained from the inverse analysis of the splitting test results (NUM$_{SPLT}$), as well as the average and envelope (experimental force – crack width curves, EXP$_{SPLT}$Avg and EXP$_{SPLT}$Envelope, respectively. As shown in Fig. 12, a good accuracy between the experimental and numerical simulation was achieved, even though a slight difference was observed, but the estimated error (*err*) was lower than 5 %.

Fig. 13 depicts the $\sigma - w$ relationship obtained from the inverse analysis that leads to the smallest error. The numerical tensile strengths for the $\theta = 0^{\circ}$ and $\theta = 90^{\circ}$ series were 3.6 and 3.2 MPa, respectively. By comparing the response for both series, similar to the uniaxial tensile test, the post-cracking residual stresses in $\theta = 0^{\circ}$ series were also significantly higher due to the fibre tendency to be reoriented perpendicular to concrete flow direction as previously discussed. Therefore, in $\theta = 0^{\circ}$ specimens there are more effective fibres to bridge the crack plane than in $\theta = 90^{\circ}$ series.

13

3.5 Comparison of results

Figs 14(a) and (b) shows for each series the uniaxial $\sigma - w$ relationships obtained from the inverse analysis procedure of the splitting tensile test (NUM_{SPLT}), the envelope and average curves from uniaxial tensile test (EXP$_{UTT}$Envelope, EXP$_{UTT}$Avg.) executed according to the RILEM TDF-162 recommendations [13]. Moreover, the $\sigma - w$ response for the splitting test was determined from Eq. 13 as recommended by ASTM C-496 standard (EXP$_{SPLT}$) [12] and is also represented in Fig. 14.

$$\sigma_{SPLT} = \frac{2F}{\pi l d} \tag{13}$$

where F is the applied line load, d is the diameter of the cylinder (150 mm) and l is the thickness of the net area in the notched plane (50 mm).

The $\sigma - w$ relationship obtained by the inverse analysis procedure rendered a relatively good approximation of the uniaxial tensile response, principally, for the series $\theta = 90°$. Regarding the $\theta = 0°$ series, NUM_{SPLT} and EXP_{SPLT} methods showed a very close numerical tensile strength, which were higher than EXP$_{UTT}$ Avg. However, as expected, splitting tensile test tends to slightly overestimate the tensile strength compared to the uniaxial tensile test. At the early cracking stages (w < 0.6 mm) NUM_{SPLT} and EXP_{SPLT} methods rendered $\sigma - w$ responses nearby upper bound limit of the EXP_{UTT} Envelope, this overestimation could be correspondent to the effects of the compressive stress along the loading plane. For higher crack opening widths, since in EXP_{SPLT} method, stress was determined from Eq. 13 that assumes a linear elastic stress distribution even after cracking of the matrix, this approach was unable to predict post-cracking tensile response with enough accuracy. On the other hand, NUM_{SPLT} started to get closer to the response obtained from the uniaxial tensile test.

Regarding the $\theta = 90°$ series (see Fig. 14(b)), the inverse analysis procedure of the splitting tensile tests also overestimated the tensile strength when compared to the tensile strength obtained from the uniaxial tests, although it was within the experimental envelope. Based on the EXP_{UTT} results, a sharp stress reduction happened once the crack initiated due to the brittle nature of the matrix and lower number of effective fibres at the fracture plane. The sudden stress decay occurred until the beginning of the hook mobilization, which happened at a crack width of around 0.3 mm. The result of the inverse analysis method reproduced the EXP_{UTT} response with a good accuracy

since unlike the $\theta = 0°$ series that showed higher residual stresses, the $\theta = 90°$ series had lower post-cracking residual stresses, therefore the load bearing capacity of the specimen has decreased and the compressive stresses were not so preponderant in the overall response.

4. CORRELATION BETWEEN THE FRACTURE AND FIBRE DISTRIBUTION PARAMETERS

Table 5 shows the fracture parameters obtained experimentally (uniaxial tensile test) and numerically (inverse analysis of splitting test) for the two series ($\theta = 0°$ and 90°). In this table, σ_{peak}, $\sigma_{0.3}$, σ_1 and σ_2 represent the stress at peak, 0.3, 1 and 2 mm, respectively; G_{F1} and G_{F2} are the dissipated energy up to a 1 and 2 mm crack opening width. It was noticeable that the influence of the notch orientation towards the concrete's flow on the post-peak behaviour of the material was quite high. The series with a notch inclination of $\theta = 0°$ revealed higher residual stresses and hence larger dissipated energy than the specimens with $\theta = 90°$. The observed variation in the post-cracking parameters could be ascribed to a preferential fibre orientation at the crack surface. On the other hand, in the casting process of the panels from the centre, since the wall effects are negligible, the flow velocity is uniform and diffuses outwards radially from the casting point, see Fig. 15. Therefore, the fibres have a tendency to reorient perpendicular to the concrete flow direction. Consequently, in the $\theta = 0°$ series because of the high number of effective fibres with favourable orientation, the composite showed a semi-hardening response while in the $\theta = 90°$ series, since fibres were rotated due to the concrete flow velocity, the number of the effective fibres was reduced and lower residual forces were achieved.

Fig. 16 depicts the relationships between the fibre distribution, N_{eff}^f, the fibre orientation factor (η_θ) and the post-cracking parameters, as well as their projection for both series obtained from the uniaxial tensile test. Since post-cracking parameters were affected by not only the fibre distribution but also the fibre orientation, it is more logical to plot these parameters versus both factors. It was observed, as expected, that the post-cracking parameters, except σ_{peak}, had a tendency to increase with the fibre orientation factor and the number of fibres bridging the fracture surface, being this effect more pronounced in the $\sigma_{0.3}$ and σ_1. To investigate the influence of each factor (N_{eff}^f or η_θ) on the post-cracking parameters, independently, in each figure, the projection of the results in the corresponding

15

plane was executed. In all figures, $\theta=0°$ specimens showed higher post-cracking parameters and also lower scattering. As it was proved from the image processing results in the previous section (Table 2), the CoVs of N_{eff}^{f} and η_θ for the $\theta=90°$ series were considerably higher than for the $\theta=0°$ series.

5. CONCLUSIONS

In this study, the influence of fibre dispersion/orientation on the tensile post-cracking parameters of steel fibre reinforced self-compacting concrete panel was investigated. The $\sigma - w$ law was determined indirectly from inverse analysis of the splitting tensile test results, as well as directly derived from the uniaxial tensile test. According to the experimental and numerical investigation, the following conclusions could be derived out:

1. The tensile behaviour of the drilled specimens from the panel was influenced by the fibre dispersion and orientation significantly. Specimens with notch direction parallel to concrete flow ($\theta=0°$) have significantly higher post-cracking residual stresses than when the notch direction was perpendicular to the flow direction ($\theta= 90°$).

2. Roughly, a linear relationship between number of the effective fibres, orientation factor and post-cracking parameters were observed. It was shown that by increasing the number of effective fibres as well as their orientation, fracture parameters tend to raise. This strong dependency could explain that in $\theta=0°$ series due to the appearing higher number of effective fibres which were mainly perpendicular to the crack plane, the concrete represented a semi-hardening behaviour, while in the other series a high stress decay was achieved.

3. In the case of casting panels from the centre, fibres have a tendency to align perpendicular to the radial flow, mainly due to the uniform flow profile velocity that diffuses outwards radially from the centre of the panel. Consequently, the total number of the effective fibres was higher in crack planes parallel towards the concrete flow ($\theta=0°$) when compared to the other case of an orthogonal crack plane towards the concrete flow ($\theta=90°$).

4. In this study it was also evidenced that the fibre orientation in a laminar specimen is completely different from the one in a prismatic specimen. In laminar specimens fibres have a tendency to re-orient perpendicular to the concrete flow direction, while in prismatic specimens the fibre's orientation tends to be parallel to the flow direction, [29,

16

30]. The determination of the tensile flexural strength of SFRC is usually performed in three-point bending tests on prismatic specimens as recommended by RILEM 162-TDF and EN-1465 [31, 32], however due to the different fibre orientation profiles in prismatic and planar structural elements, it could lead to an unrealistic tensile behaviour of laminar structural elements like panels, shells or walls.

5. The inverse analysis of the splitting tensile response can estimate with a relatively good accuracy the uniaxial tensile behaviour, in particular, for low fibre contents. In general, in the case of using a relatively high content of fibres, which lead to either a partial or full pseudo-hardening behaviour (as it was the case of the $\theta=0^{\circ}$ series), the proposed methodology could somehow overestimate the $\sigma - w$ law. In this case it is preferable to use a modified version of the splitting tensile test similar to the one proposed by di Prisco *et al.* [33].

ACKNOWLEDGEMENTS

REFERENCES

[1] ACI 544–1R, 2002, State-of-the-art report on fiber reinforced concrete, Technical report, American Concrete Institute, (2002).

[2] Balaguru, P.N., Shah, S.P., Fiber reinforced cement composites, McGraw-Hill Inc., New York, (1992).

[3] Vandewalle, L., Dupont, D., Bending test and interpretation, test and design methods for steel fibre reinforced concrete, background and Experiences, RILEM publication PRO 31, Bagneux, (2003) 1-14.

[4] Banthia, N., Trottier, J., Concrete reinforced with deformed steel fibres, Part I: Bond-slip mechanisms, ACI Materials Journal, 91(1994) 435-446.

[5] Cunha, V.M.C.F., Barros,J.A.O., Sena-Cruz,J.M., Pullout behaviour of Steel Fibres in Self Compacting Concrete, ASCE Journal of Materials in Civil Construction, 22 (2010) 1-9.

[6] Laranjeira, F., Design-oriented constitutive model for steel fiber reinforced concrete, PhD thesis, Universitat Politècnica de Catalunya, (2010).

[7] Ferrara, L., Meda, A., Relationships between fibre distribution, workability and the mechanical properties of SFRC applied to precast roof elements, Materials and Structures, 39 (2006) 411-420.

[8] Pansuk, W., Sato, H., Sato, Y., Shionaga, R., Tensile behaviours and fibre orientation of UHPC, In Proceedings of Second International Symposium on Ultra High Performance Concrete, Kassel, Germany (Kassel University Press), (2008) 161-168.

[9] Kim, S.W., Kang, S.T., Park, J.J., Ryu, G.S., Effect of filling method on fibre orientation and dispersion and mechanical properties of UHPC, Proceedings of Second International Symposium on Ultra High Performance Concrete, Kassel, Germany (Kassel University Press), (2008) 185-192.

[10] EFNARC, The European guidelines for self-compacting concrete, (2005).

[11] Barnett, S.J., Lataste, J.F., Parry, T., Millard, S.G., Soutsos, M.N., Assessment of fiber orientation in ultra high performance fibre reinforced concrete and its effects on flexural strength, Materials and Structures, 43 (2010) 1009-1023.

[12] ASTM C496, Standard test method for splitting tensile strength of cylindrical concrete specimens, Annual Book of ASTM Standards, American Society of Testing Materials, (2004).

[13] RILEM TC162-TDF, Test and design methods for steel fibre reinforced concrete: Uniaxial tension test for steel fibre reinforced concrete, Materials and Structures, 34 (2001) 3-6.

[14] Cunha, V.M.C.F., Barros, J.A.O., Sena-Cruz,J.M., An integral approach for modeling the tensile behaviour of steel fibre reinforced self-compacting concrete, Cement and Concrete Research, 41 (2011) 64-76.

[15] Kang, S.T., Kim,J.K., The relation between fibre orientation and tensile behavior in an Ultra High Performance Fibre Reinforced Cementitious Composites (UHPFRCC), Cement and Concrete Research, 41 (2011) 1001-1014.

[16] Ferrara, L., Ozyurt, N., Di Prisco, M., High mechanical performance of fiber reinforced cementitious composites - the role of casting-flow induced fiber orientation, Materials and Structures, 44 (2011) 109-128.

[17] Rasband, W., ImageJ, National Institutes of Health, USA, (2008).http://rsb.info.nih.gov/ij/

[18] KamerwaraRao, C.V.S., Effectiveness of random fibres in composites, Cement and Concrete Research, 9 (1979) 685-693.

[19] Stroeven, P., Hu, J., Effectiveness near boundaries of fibre reinforcement in concrete, Materials and Structures, 39 (2006) 1001-1013.

[20] Abrishambaf, A., Barros, J.A.O., Cunha, V.M.C.F., A state of art on the fibre orientation and distribution in steel fibre reinforced concrete, Report no. 13-DEC/E-16, University of Minho, Guimaraes, Portugal, (2013) 26-31.

[21] Laranjeira, F., Grunewald,S., Walraven,J., Blom,C., Molins,C., Aguado, A., Characterization of the orientation profile of steel fiber reinforced concrete, Materials and Structures, 14 (2010) 1093-1111.

[22] Zhou, F.P., Some aspects of tensile fracture behaviour and structural response of cementicious materials, Report no. tvbm-1008, division of building materials, Lund Institute of Technology, Lund, Sweden, (1988).

[23] Abaqus Unified FEA software, User Manual, Dassault Systèmes Simulia Corp., Providence, RI, USA, (2009).

[24] Abaqus Unified FEA software, Analysis user's manual, Volume IV: Elements, Dassault Systèmes Simulia Corp., Providence, RI, USA, (2009).

[25] Abaqus Unified FEA software, Analysis user's manual, Volume III: Materials, Dassault Systèmes Simulia Corp., Providence, RI, USA, (2009).

[26] Lubliner, J., Oliver, J., Oller, S., Onate, E., A plastic-damage model for concrete, International Journal of Solids Structures, 25 (1989) 299-329.

[27] Jankowiak, T., Lodygowski, T., Identification of parameters of concrete damage plasticity constitutive model, Foundations of Civil and Environmental Engineering, 6 (2005) 53-69.

[28] Kmiecik, P., Kaminski, M., Modeling of reinforced concrete structures and composite structures with concrete strength degradation taken into consideration, Archives of Civil and Mechanical Engineering, 11 (2011) 623-636.

[29] Martinie, L., Roussel, N., Simple tools for fiber orientation in industrial practice, Cement and Concrete Research, 41 (2011) 993-1000.

[30] Stähli, P., Custer, R., On flow properties, fibre distribution, fibre orientation and flexural behaviour of FRC, Materials and Structures, 41 (2008) 189-196.

[31] RILEM TC162-TDF, Test and design methods for steel fibre reinforced concrete: Bending test. Materials and Structures, 33 (2000) 75-81.

[32] EN 14651, Test method for metallic fibered concrete - Measuring the flexural tensile strength (limit of proportionality (LOP), residual), European Committee for Standardization, Brussels, (2005).

[33] di Prisco, M., Ferrara, L., Lamperti, M.G.L., Double edge wedge splitting (DEWS): an indirect tension test to identify post-cracking behaviour of fibre reinforced cementitious composites. Materials and Structures, 46 (2013) 1893-1918.

FIGURES AND TABLES

List of Figures:

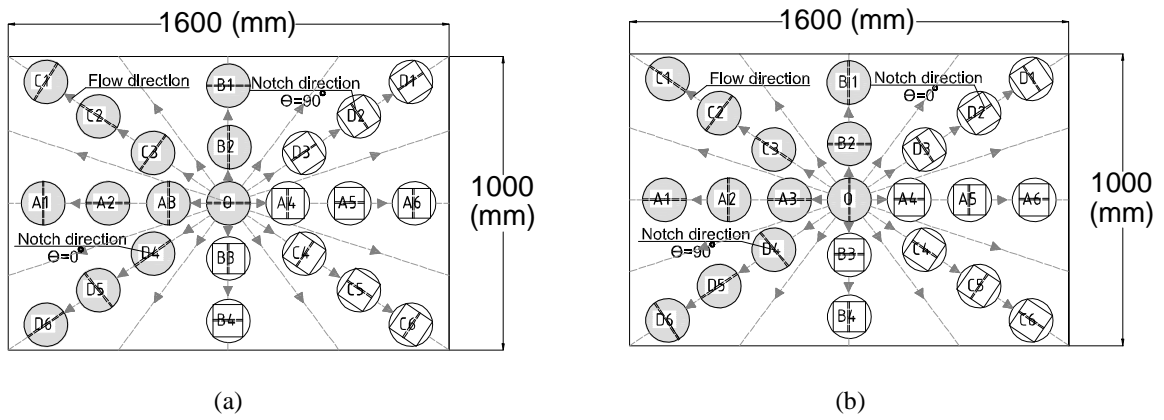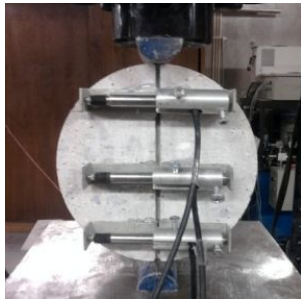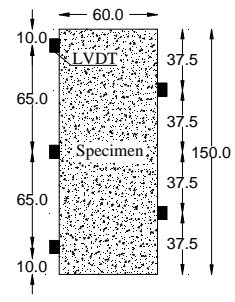Figure 1: Core extracting plan: (a) panel A, (b) panel B.

Figure 2: Geometry of the specimen and setup of the splitting tensile test (dimensions are in mm): (a) specimen front view (top of the panel), (b) specimen lateral view.
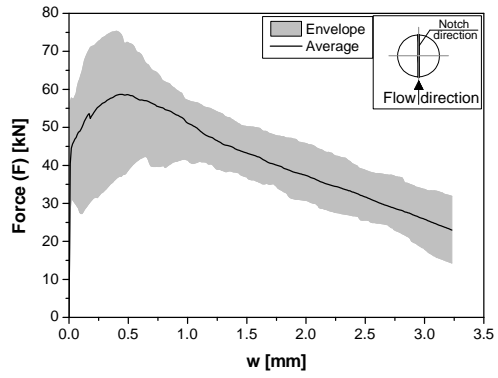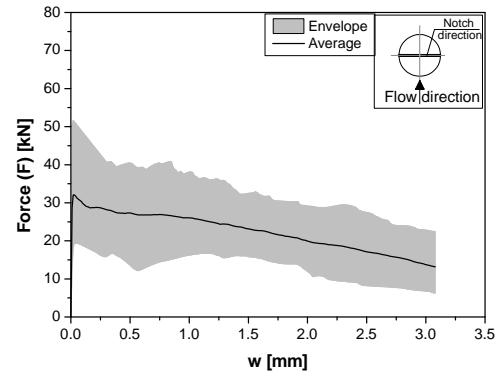
Figure 3: Uniaxial tensile test setup: (a) specimen front view, (b) specimen lateral view (units in mm).
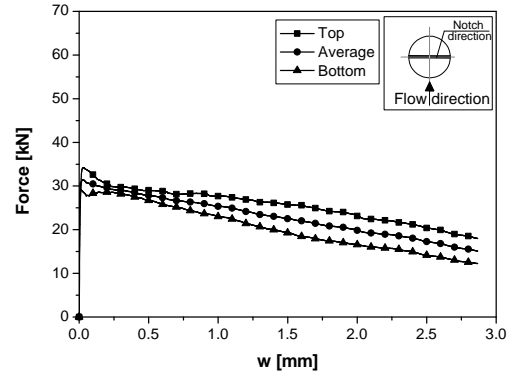
Figure 4: Force – crack opening width relationship, $F – w$, obtained from splitting tensile test for: (a) $\theta=0^{\circ}$ and (b) $\theta = 90^{\circ}$.

Figure 5: Nominal tensile stress – crack opening width relationship, $\sigma – w$, obtained from splitting tensile test for the two sides (top and bottom) of the specimens: (a) $\theta = 0^{\circ}$ and (b) $\theta = 90^{\circ}$.

Figure 6: Force – average crack width relationship, $F- w$, obtained from the uniaxial tensile tests: (a) $\theta = 0^{\circ}$ and (b) $\theta = 90^{\circ}$.
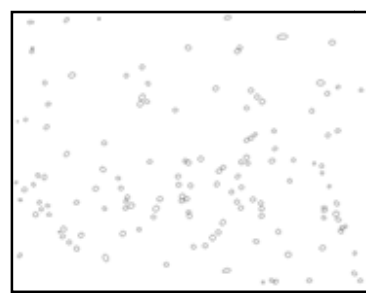
Figure 7: Image processing steps: (a) converting a colored image to greyscale image (b) adjusting a threshold, (c) defining mask, noise (remove small noises) and watershed (separated fibres that are stuck together) functions, (d) fitting the best ellipse to each fibre.

Figure 8: Localization of the plane surface considered in the fibre distribution assessment (units in mm).

Figure 9: Predicted orientation profile: (a) $\theta=0^{\circ}$ and (b) $\theta=90^{\circ}$.

Figure 10: Number of the fibres, N^{f}, versus number of the effective fibres, N^{f}_{eff}.

Figure 11: Three-dimensional view of numerical model [24]: (a) geometry, constraints and prescribed displacement, (b) finite element mesh.

Figure 12: Experimental and numerical force – crack width relationship, $F-w$, for: (a) $\theta=0^{\circ}$ and (b) $\theta = 90^{\circ}$.

Figure 13: Numerical uniaxial stress – crack width relationship, $\sigma – w$, obtained from inverse analysis for: (a) $\theta=0^{\circ}$ and (b) $\theta = 90^{\circ}$.

Figure 14: Comparison of the uniaxial stress – crack width relationship, $\sigma – w$, for: (a) $\theta=0^{\circ}$ and (b) $\theta = 90^{\circ}$.

Figure 15: Explanation for fibre alignment in flowing concrete of a panel casting from the centre.

Figure 16: Relationship between the fibre distribution, the fibre orientation factor and the post-cracking parameters: (a) peak stress, (b), (c) and (d) stress at a 0.3, 1 and 2 mm crack width, respectively; (e) and (f) energy absorption up to 1 and 2 mm crack width, respectively.

List of Tables:

Table 1: Mix composition of steel fibre reinforced self-compacting concrete per m^3.

Table 2: Fibre distribution parameters.

Table 3: The constitutive parameters of CDP model.

Table 4: Mechanical properties adopted in the numerical simulations.

Table 5: Residual stress and toughness parameters obtained from different analysis.

Figure 1: Core extracting plan: (a) panel A, (b) panel B.

(a)   (b)

Figure 2: Geometry of the specimen and setup of the splitting tensile test (dimensions are in mm): (a) specimen front view (top of the panel), (b) specimen lateral view.
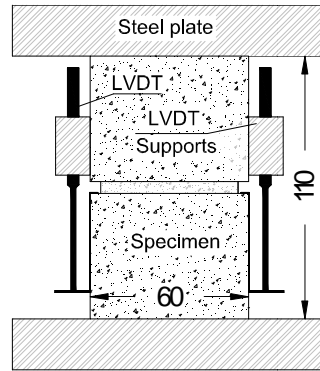
(a)   (b)

Figure 3: Uniaxial tensile test setup: (a) specimen front view, (b) specimen lateral view (units in mm).

(a)

(b)

Figure 4: Force – crack opening width relationship, $F – w$, obtained from splitting tensile test for: (a) $\theta=0^{\circ}$ and (b) $\theta = 90^{\circ}$.
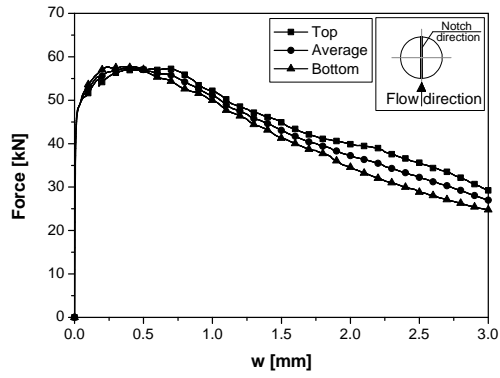
(a)

(b)

Figure 5: Nominal tensile stress – crack opening width relationship, σ– w, obtained from splitting tensile test for the two sides (top and bottom) of the specimens: (a) $\theta = 0^{\circ}$ and (b) $\theta = 90^{\circ}$.
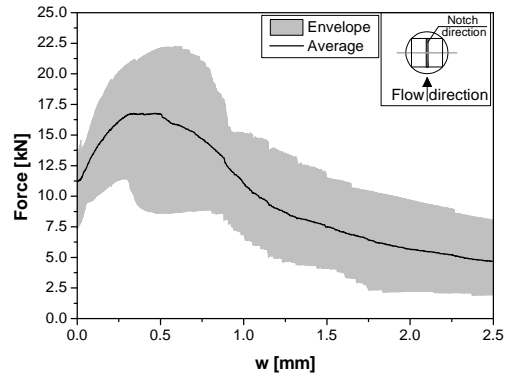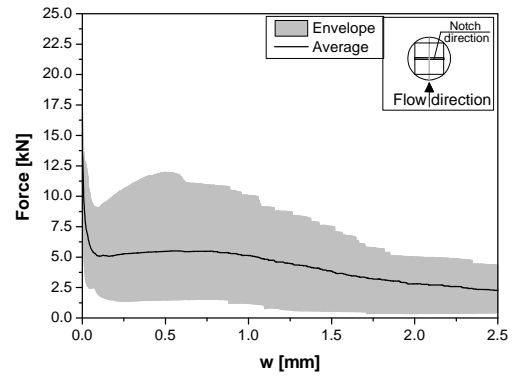
(a)   (b)

Figure 6: Force – average crack width relationship, F- w, obtained from the uniaxial tensile tests: (a) $\theta = 0°$ and (b) $\theta = 90°$.
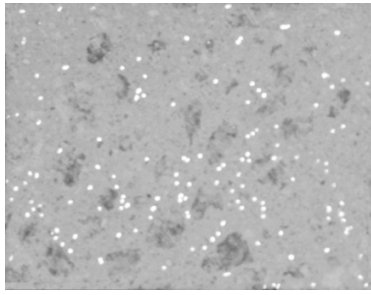
(a)　　　　　　　　　　　　　　　　　　　(b)
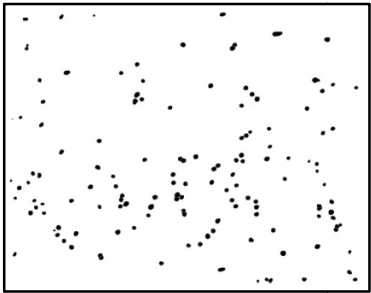
(c)　　　　　　　　　　　　　　　　　　　(d)

Figure 7: Image processing steps: (a) converting a colored image to greyscale image (b) adjusting a threshold, (c) defining mask, noise (remove small noises) and watershed (separated fibres that are stuck together) functions, (d) fitting the best ellipse to each fibre.
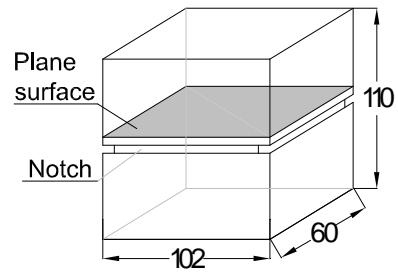
Figure 8: Localization of the plane surface considered in the fibre distribution assessment (units in mm).
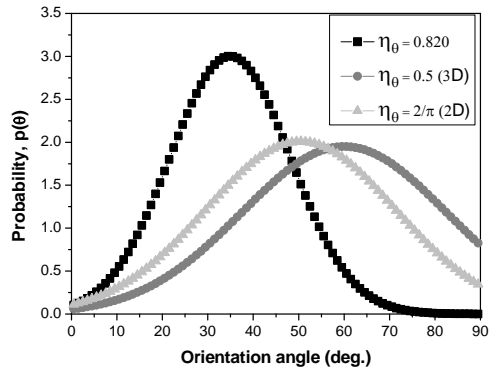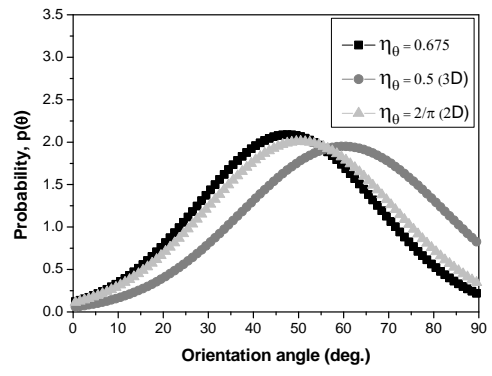
Figure 9: Predicted orientation profile: (a) $\theta=0°$ and (b) $\theta=90°$.
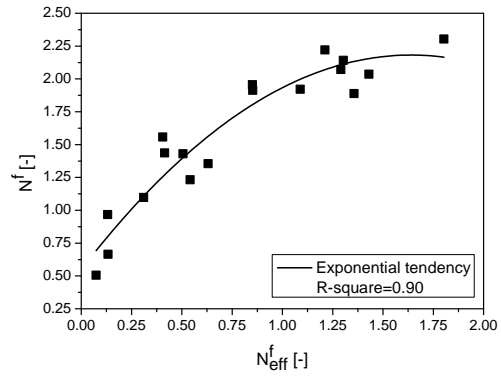
Figure 10: Number of the fibres, N^f, versus number of the effective fibres, N_{eff}^f.
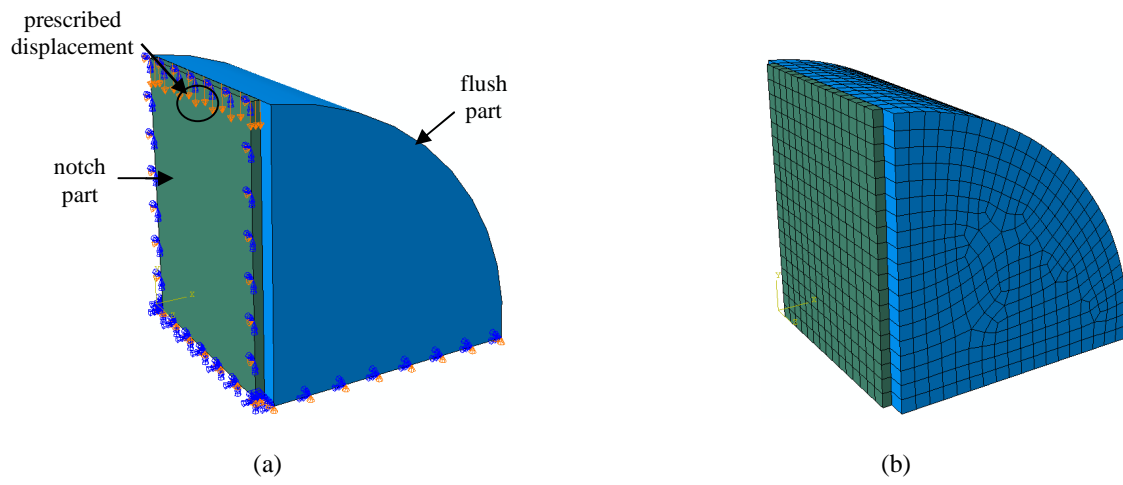
Figure 11: Three-dimensional view of numerical model [24]: (a) geometry, constraints and prescribed displacement, (b) finite element mesh.
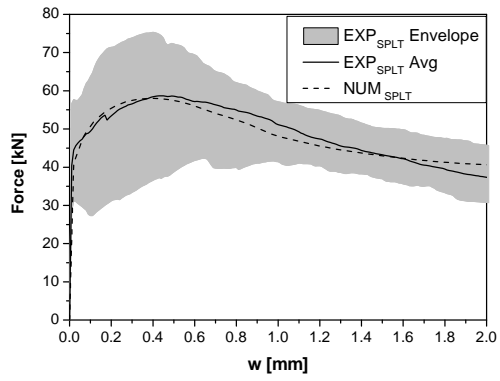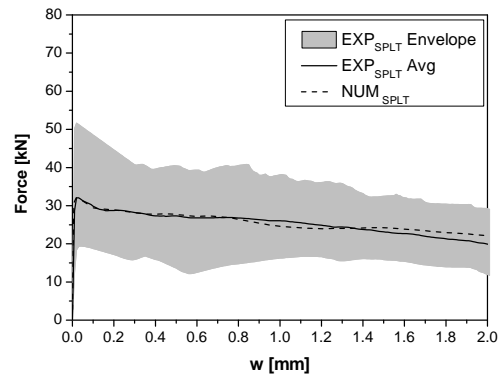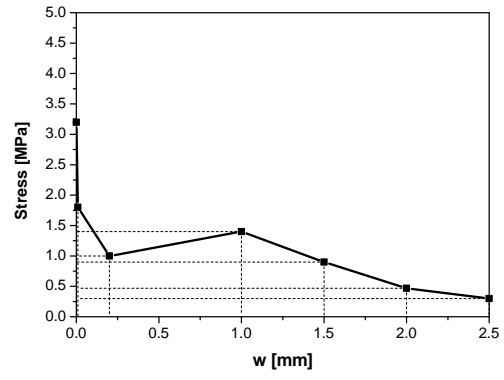
(a)   (b)

Figure 12: Experimental and numerical force – crack width relationship, *F-w*, for: (a) $\theta=0^{\circ}$ and (b) $\theta = 90^{\circ}$.
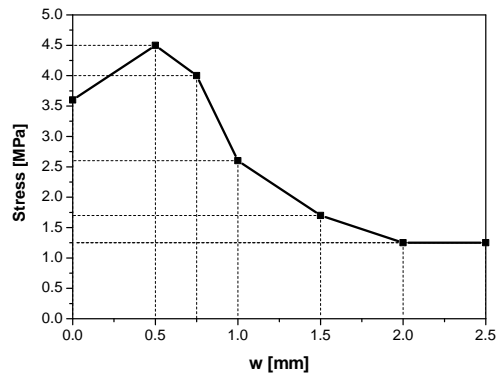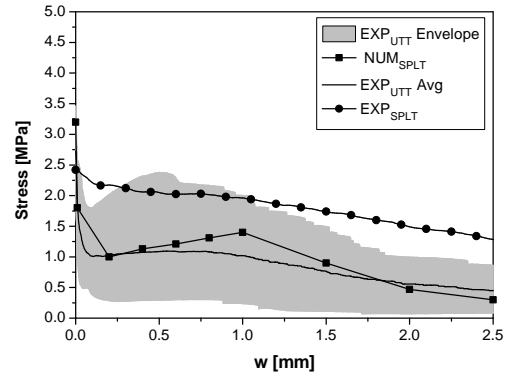
(a)   (b)

Figure 13: Numerical uniaxial stress – crack width relationship, σ – w, obtained from inverse analysis for: (a) $\theta=0°$ and (b) $\theta = 90°$.
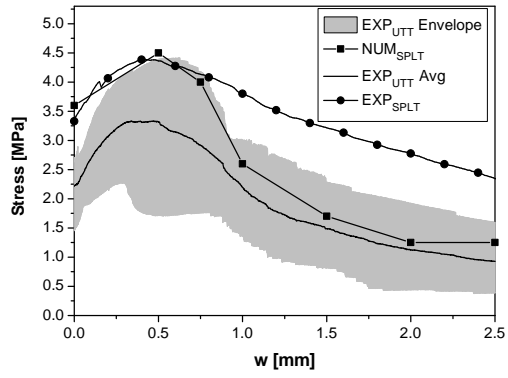
(a)

(b)

Figure 14: Comparison of the uniaxial stress – crack width relationship, $\sigma - w$, for: (a) $\theta=0°$ and (b) $\theta = 90°$.
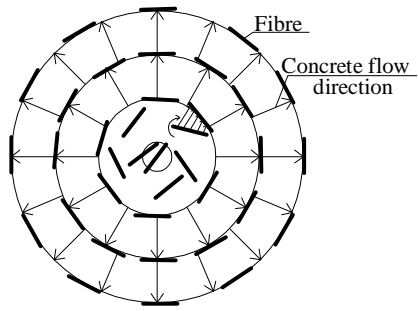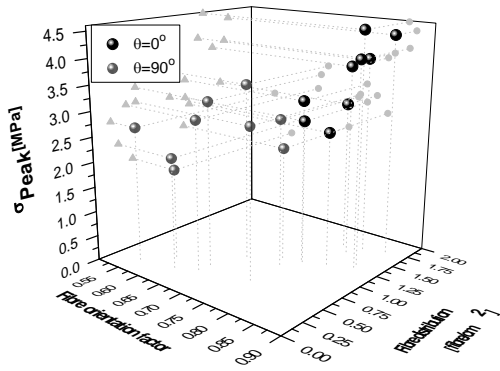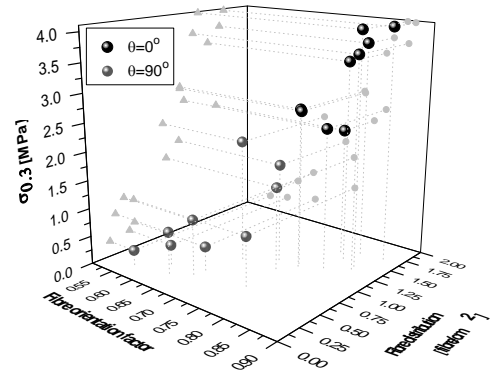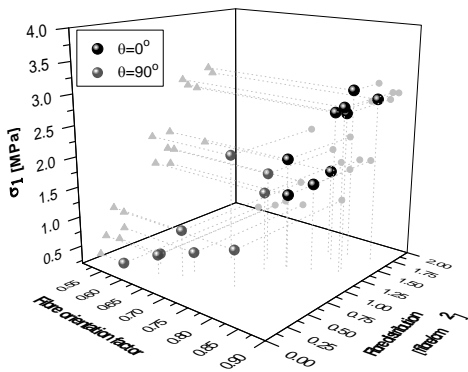
Figure 15: Explanation for fibre alignment in flowing concrete of a panel casting from the centre.
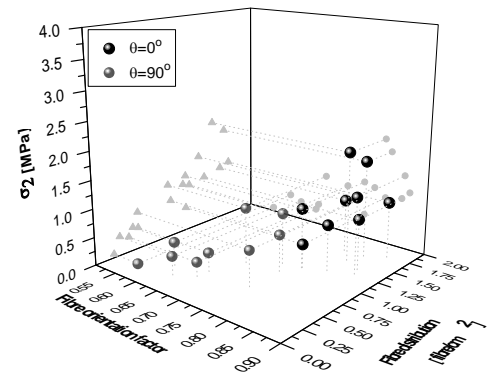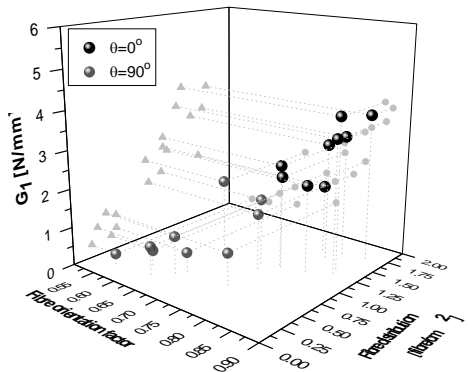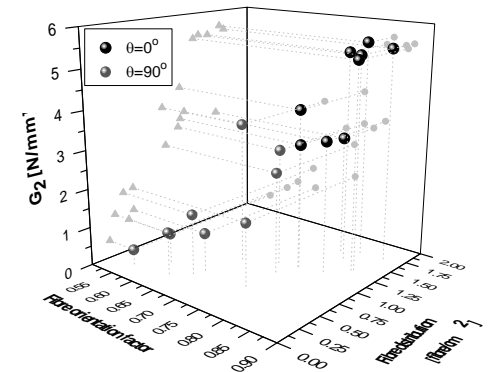
(a)

(b)

(c)

(d)

(e)

(f)

Figure 16: Relationship between the fibre distribution, the fibre orientation factor and the post-cracking parameters: (a) peak stress, (b), (c) and (d) stress at a 0.3, 1 and 2 mm crack width, respectively; (e) and (f) energy absorption up to 1 and 2 mm crack width, respectively.

Table 1: Mix composition of steel fibre reinforced self-compacting concrete per m^3.

C	W	SP	F	FS	CS	CA	Fibre
[kg]	[kg]	[kg]	[kg]	[kg]	[kg]	[kg]	[kg]
413	140	7.83	353	237	710	590	60

Table 2: Fibre distribution parameters.

Specimen	Distance [cm]	$\theta=0°$				$\theta=90°$			
		N^f [fibres/cm^2]	N^f_{eff} [fibres/cm^2]	η_θ [-]	ξ_{seg} [-]	N^f [fibres/cm^2]	N^f_{eff} [fibres/cm^2]	η_θ [-]	ξ_{seg} [-]
B3	20.0	2.071	1.291	0.827	0.580	1.557	0.405	0.688	0.476
A4	23.5	1.889	1.356	0.855	0.518	1.430	0.506	0.737	0.510
C4	32.0	2.036	1.430	0.851	0.555	0.665	0.133	0.630	0.597
D3	32.0	1.913	0.853	0.775	0.491	1.436	0.415	0.666	0.586
B4	40.0	1.956	0.851	0.773	0.530	0.506	0.074	0.561	0.643
A5	46.5	2.220	1.212	0.814	0.479	1.097	0.311	0.672	0.725
A6	69.5	2.304	1.803	0.866	0.557	0.967	0.132	0.604	0.539
C6	77.5	2.142	1.303	0.818	0.600	1.232	0.541	0.756	0.485
D1	77.5	1.921	1.089	0.795	0.532	1.355	0.631	0.760	0.594
Average		2.050	1.24	0.820	0.538	1.138	0.35	0.675	0.573
CoV (%)		7.16	23.74	4.15	7.33	31.98	57.11	10.20	14.00

Table 3: The constitutive parameters of CDP model.

Dilatation angle [degrees]	40
Eccentricity, e [-]	0.1
σ_{bo}/σ_{co}[-]	1.16
K_c [-]	0.667

Table 4: Mechanical properties adopted in the numerical simulations.

Density, ρ	2.4×10^6 N/mm^3
Poisson ratio, υ	0.2
Initial young modulus, E_{cm}	34.15 N/mm^2
Compressive strength, f_{cm}	47.77 N/mm^2
Tensile strength	Inverse analysis
Post-cracking parameters	Inverse analysis

Table 5: Residual stress and toughness parameters obtained from different analysis.

Series	Parameter	σ_{peak} [MPa]	$\sigma_{0.3}$ [MPa]	σ_1 [MPa]	σ_2 [MPa]	G_{F1} [N/mm]	G_{F2} [N/mm]
$\theta = 0°$	NUM$_{SPLT}$	4.50	4.10	2.60	1.25	3.91	6.35
($\sigma_{\parallel}$)	EXP$_{UTT}$	3.33	3.24	2.30	1.14	2.94	4.47
$\theta = 90°$	NUM$_{SPLT}$	3.20	1.06	1.40	0.47	1.26	2.18
($\sigma_{\perp}$)	EXP$_{UTT}$	2.72	1.05	1.02	0.56	1.09	1.86